Analysis of Microseismicity and Reactivated Fault Size to Assess the Potential for Felt Events by CO_2 Injection in the Illinois Basin

Sherilyn Williams-Stroud*[1], Robert Bauer[1], Hannes Leetaru[1], Volker Oye[2], Frantisek Stanek[3,4], Sallie Greenberg[1], and Nadege Langet[2]

ABSTRACT

The results of monitoring of carbon dioxide (CO_2) injection at the Illinois Basin—Decatur Project (IBDP) and the companion Illinois Industrial Carbon Capture and Sequestration Sources (IL-ICCS) project—have shown that reservoir response to fluid pressure changes can vary significantly at different injection locations within the same reservoir. Predrill reservoir characterization is important to identify potentially seismogenic faults. However, interpretations of newly reprocessed 3D seismic reflection data illustrate the challenges related to their identification in a region dominated by faulting with small vertical offsets. Faults interpreted in the 3D seismic volume range from ~300 to 1200 m wide and are in the same size range as faults that could have been the source of historical events up to M_w 2.7 in central Illinois. The array of monitoring sensors that was installed for the IBDP continues to collect data, as injection operates in IL-ICCS, the second injection well. CO_2 injection rates for the IL-ICCS well are on average 1.7 times the rates injected in the IBDP well, but a significantly reduced rate of induced seismicity is observed. This article presents results of passive seismic monitoring for the duration of the project to date, integrating active and passive seismic data to develop a new interpretation of the subsurface structure at the Decatur site that explicitly identifies pathways for fluid flow into the basement leading to induced seismicity, and provides a geological explanation for the sharp reduction of induced seismicity during injection at higher rates into the second well. The use of seismic moment to estimate the length of seismogenic slip planes in the local subsurface suggests that faults large enough to produce felt seismicity are unlikely to be present at or near the Decatur site.

KEY POINTS

- We estimate potential earthquake sizes from CO_2 injection at a central United States site using geologic information.
- Geologic setting, preinjection fault characterization, and reservoir quality are needed for these estimates.
- Geologic information may provide insights as to whether large induced events are likely or not.

Supplemental Material

INTRODUCTION

The Illinois Basin–Decatur Project (IBDP) and the Illinois Industrial Carbon Capture and Sequestration Sources (IL-ICCS) projects have injected 2.8 million tonnes of CO_2 into a 500 thick saline sandstone reservoir at a depth of 2140 m. Injection into the base of the Mt. Simon sandstone began in November 2011 at the CCS1 well and was stopped in November 2014 after injection of 999,215 tonnes (Bauer *et al.*, 2019). Twenty-eight months after operations ceased in the first well, injection began in the CCS2 well at 50 m shallower depth and with average wellhead pressure of 12 MPa. As of April 2020, 1.8 million tonnes of CO_2 has been injected into CCS2, bringing the total injected into both wells to nearly 2.8 million tonnes. Passive seismic monitoring has been continuous at the site, starting 564 days prior to injection. Over 68,000 seismic events were recorded during that period, but most were related to drilling activities and other well operations, with about 1100 distant events considered to be related to quarry or mine blasting operations (Smith and Jaques, 2016). One dozen distant events correlated in time to events in the U.S. Geological Survey (USGS) earthquake catalog. Eight events were interpreted to be local

1. Illinois State Geological Survey, Champaign, Illinois, U.S.A.; 2. NORSAR, Kjeller, Norway; 3. Seismik s.r.o., Prague, Czech Republic; 4. Institute of Rock Structure and Mechanics of the Czech Academy of Sciences, Prague, Czech Republic

*Corresponding author: sherilyn@illinois.edu; swilliamsstroud@gmail.com

Cite this article as Williams-Stroud, S., R. Bauer, H. Leetaru, V. Oye, F. Stanek, S. Greenberg, and N. Langet (2020). Analysis of Microseismicity and Reactivated Fault Size to Assess the Potential for Felt Events by CO_2 Injection in the Illinois Basin, *Bull. Seismol. Soc. Am.* **XX**, 1–17, doi: 10.1785/0120200112

microseismic events not related to drilling operations and indicative of the natural background seismicity level at the site. After the start of injection, nearly 20,000 detected and more than 5000 locatable events have been recorded, with magnitudes ranging from −2.1 to 1.2 (as detected by the downhole array), and no felt seismicity was associated with this project.

Prior knowledge of the presence of faults susceptible to earthquake-inducing slip is crucial for assessing seismic hazard, and predictions of ground motion have become more important, as the connection to human activity continues to be identified. The spatial distribution of the microseismicity clusters indicates reactivation of faults in and beneath the reservoir (Goertz-Allmann *et al.*, 2017; Bauer *et al.*, 2019), some of which are spatially coincident with faults interpreted in the reprocessed seismic data. Couëslan, Butsch, *et al.* (2014) named event clusters by the order in which events first appear in each location over time, identifying 18 different clusters that developed during CCS1 injection.

Wastewater disposal operations in, for example, Oklahoma and Kansas, hydraulic fracturing activities in western Canada, and geothermal operations in northern California, South Korea, and Switzerland have been associated with felt and sometimes damaging earthquakes. In contrast, felt seismicity has not been reported as a result of CO_2 injection activities (Rinaldi *et al.*, 2014). Because of the goal of long-term injection and containment of large volumes, the public perception of the similarity to wastewater injection, for which some of the largest injection-induced earthquakes have been reported, needs to be addressed. Whether CO_2 injection will lead to significant felt seismicity is still not known.

Microseismic events have been detected only at the few sites with commercial injection rates of ∼1 Mt/yr or more. Injection at the Weyburn Field in Saskatchewan, Canada, produced more than 200 locatable events with magnitude range −3.5 to −0.5 (Verdon, 2016). Over 5000 microseismic events ($M_w \leq 1$) were detected during the injection of CO_2 at the In Salah Carbon Capture and Storage site in the Krechba Field, Algeria, even though the monitoring configuration was significantly limited with only two geophones in a monitoring well at about 80 m depth (Goertz-Allmann *et al.*, 2014). Stork *et al.* (2014) reported maximum event magnitude at the Algeria site as M_w 1.7, and there were no reports of felt seismicity.

Restricting comparisons to CO_2 injection only, the IBDP was able to record significantly more induced seismicity than two other projects that injected CO_2 at commercial rates, the In Salah CCS site, and the Weyburn Enhanced Oil Recovery site. The difference in the number of detected events between sites may be influenced by the number and placement of sensors, vertical separation from the injection layer, and distances and distribution of injection wells in relation to the geophone(s). The largest event magnitudes at IBDP and In Salah are comparable and larger than at Weyburn. The small vertical offset faults in the subsurface at the IBDP and IL-ICCS site are difficult to identify in active seismic imaging. In contrast, faults at In Salah are more easily identified, measuring 2 km or more (Goertz-Allman *et al.*, 2014, see Fig. 1), and additional geological factors, such as lithology, thickness, and reservoir in situ stress likely also contributed to differences in reservoir response at the two sites.

Because monitoring has taken place continuously at the IBDP site, it is possible to observe changes in the microseismicity from injection in the first well (CCS1) and from injection in the second well (CCS2) as well as the reservoir response during the period when no injection was taking place. A significant reduction in seismicity has occurred despite the 1.7-fold increase in the injection rate, with the number of microseismic events being comparable to the level observed during the noninjection period between CCS1 and CCS2 injections.

This article discusses the influence of the following analyses on reservoir characterization efforts at IBDP: reprocessed seismic reflection volume and porosity inversion, subsurface pressure monitoring results, and focal mechanism analysis on 50 microseismic events. A fault-size analysis is combined with fault-size estimates calculated from event seismic moment to further constrain the size distribution of existing faults in the reservoir and assess the likelihood of felt seismicity from CO_2 injection. The data collected while no injection operations were active and after injection in the second well provided additional information to support and enhance the subsurface interpretation.

Faults that were not visible in the first processing of the volume are interpretable in the reprocessed volume, which helped to confirm the existence of faulting in some of the locations where microseismicity was detected and helped to identify previously unrecognized stratigraphic relationships that influence pressure propagation. The lack of strong reflectors in the basement rocks inhibits fault interpretation in the reprocessed volume as well, but the improved imaging of the reservoir rocks increased our confidence for interpreting faults that extend from the overlying rocks into the basement. The passive seismic monitoring data collected, after the CCS1 well was shut in, are described for the first time in this study, with discussion of those results with respect to the updated geological and structural interpretation. These interpreted faults are similar in size to possible faults indicated by microseismicity, ranging from 100 m mapped length to 1200 m for the largest faults. Estimates of fault sizes calculated from event seismic moment using relationships by McGarr and Fletcher (2003) and Thingbaijam *et al.* (2017) are also similar to the sizes of the interpreted faults associating $M_w \sim 1$ events with fault or failure planes ranging from 500 to 1000 m in length. The very different reservoir response to two different injection wells showed that relatively small changes in well location and injection interval can significantly impact the injection response.

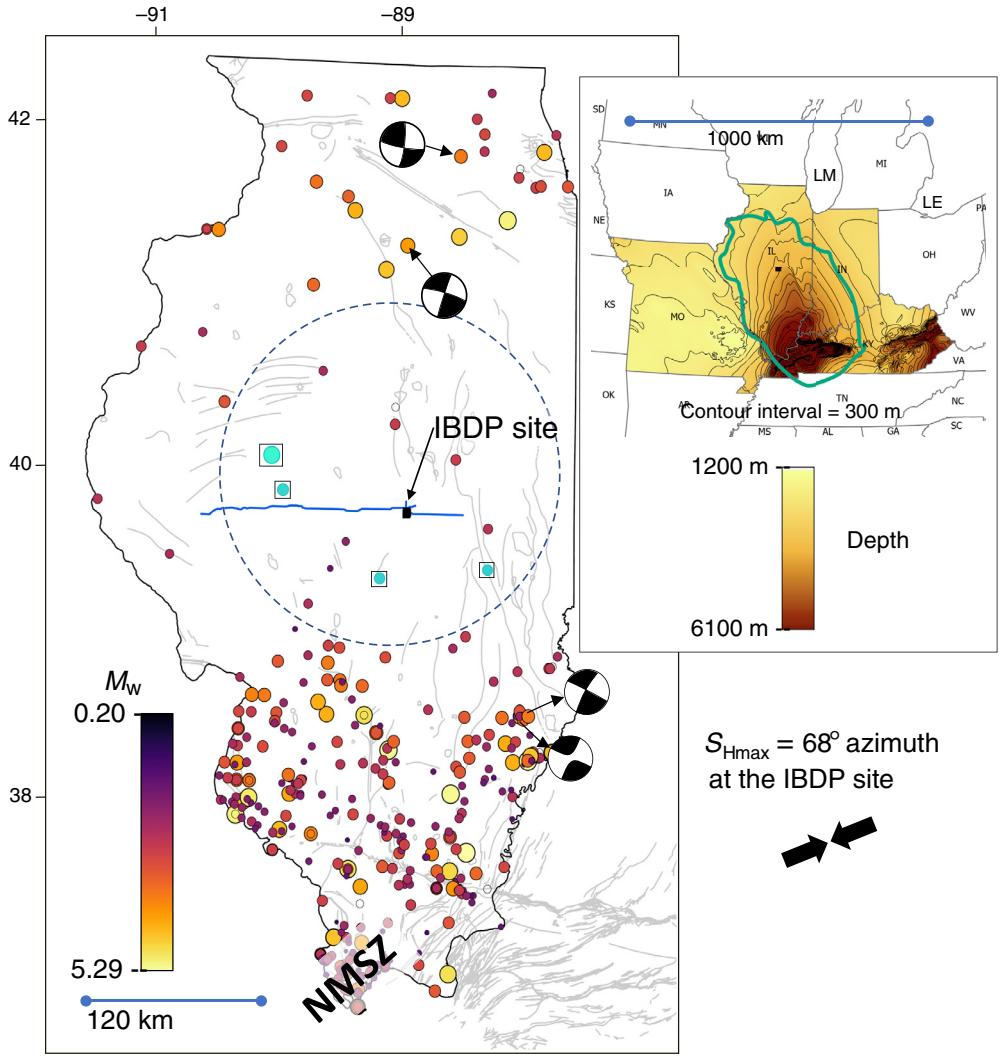

Figure 1. Location map of the Illinois basin in the north-central United States. The inset map shows the depth to Precambrian basement in the states Missouri, Illinois, and Indiana. The green polygon is the outline of the Illinois basin. The map on the left shows historical seismicity in Illinois from the Illinois State Geological Survey (ISGS) catalog of earthquakes reported and detected from 1795 to 2017. The four largest earthquakes within 100 km of the Decatur site are displayed as boxed circles. Source mechanisms determined by the U.S. Geological Survey (USGS) for some earthquakes are shown near their epicenters. The area in the south labeled New Madrid seismic zone (NMSZ) corresponds to the northern part of the NMSZ. The small black box in the central part of the state indicates the approximate location of the Illinois Basin–Decatur Project (IBDP), shown with intersecting 2D seismic acquisition lines. Fault lines (light gray) include faults from all depths as mapped from surface and subsurface information. LE, Lake Erie; LM, Lake Michigan. The color version of this figure is available only in the electronic edition.

In this case, changing the injection interval of the well led to a starkly lower microseismicity response, despite the higher injection rate.

PROJECT DESCRIPTION

The IBDP is a large-scale demonstration project for integrated carbon capture and geological storage in a saline reservoir conducted at the Archer Daniels Midland (ADM) Company's corn processing plant in Decatur, Illinois. The project is the first example of a bioenergy CCS project and is led by the Midwest Geological Sequestration Consortium at the Illinois State Geological Survey (ISGS) with funding from the U.S. Department of Energy—National Energy Technology Laboratory. Nearly 1 million tonnes of CO_2 were injected into the base of a 500 m thick saline sandstone reservoir at a depth of 2140 m for more than 3 yr from November 2011 to 2014 in the CCS1 well. Prior to injection, an extensive investigation of site conditions included monitoring of air, soil, groundwater, and bedrock. Monitoring activities are scheduled to continue into the first quarter of 2021. A second injection well, CCS2, part of the IL-ICCS project, was brought online in April 2017. As a result, data collection also encompasses induced seismicity related to the IL-ICCS industrial-scale demonstration project. Injection in the CCS2 well is scheduled to take place for 3 yr or longer, with a total injection volume target of up to 5 million tonnes, and its average rate to date is about 570,000 tonnes/yr.

Reservoir modeling and risk assessment were priority goals for the IBDP, including extensive monitoring, verification, and assessment activities. Establishing the National Carbon Sequestration Education Center at Richland Community College in Decatur, Illinois, provided a venue where the public can learn about the science and technology of CCS and an educational pathway for students who are interested in CCS careers. The IBDP also served as a testbed for existing and new technologies, such as wellbore monitoring engineering design advancements.

Geological setting

The Illinois basin is a broad, spoon-shaped depression (380 km wide and 650 km long at the maximum extents) that spans

most of Illinois, and parts of Indiana and Kentucky (Fig. 1). The deepest part of the basin is to the south, where structure is also significantly more complex. The southern end of the Illinois basin, near the border with Kentucky and Missouri, includes the Wabash Valley seismic zone and intersects the seismically active New Madrid seismic zone. Felt natural earthquakes occur in the southern parts of Illinois and in some counties in the northern part of Illinois, but they are rare in the central part of the state. Since 2002, 36 felt events in 19 counties have been recorded in Illinois, all tied to faults in basement rock. Subsurface data are more extensive for southern Illinois because of energy industry activities. Faults have been mapped through underground coal mines and identified using data from the high density of oil and gas wells. Historical seismicity (since 1795), determined from local newspaper account descriptions of damage, has a similar earthquake occurrence distribution. Approximately 90% of historical earthquakes occurred in southern Illinois. Only four (likely) felt ($M_w > 3$) events were reported within approximately 100 km of the Decatur site since 1908 and recent revisions of the estimated magnitudes of those events in the Central Eastern United States–Seismic Source Characterization earthquake catalog lowered all of the moment magnitudes of these events, so that three of these events now have estimated $M_w < 3$. The revised magnitude of the closest event, 45 km to the south of the injection site, is estimated as M_w 2.7. The largest of these four events is also the farthest away (103 km west-northwest), with original estimated M_w 4.8 and revised M_w 4.4. Mapped faults in southern Illinois can reach the surface, and many are interpreted to be tens of kilometers long in subsurface data from seismic imaging, reflecting a complicated structural history in this area. Several distinct deformation phases have been identified (Potter *et al.*, 1997; Duchek *et al.*, 2004). Seismic reflection imaging shows that deformation and faulting in central Illinois is less intense than in the southern parts of the state, as fault displacements are more frequently large enough in southern Illinois to be easily identifiable in seismic data. Historical seismicity is also spatially correlated with the increasing structural complexity of southern Illinois. The Decatur site is located near the center of an area that is relatively free of historical seismicity within approximately 100 km, suggesting that large faults on which felt earthquakes can occur are not present.

Four representative source mechanisms from naturally occurring earthquakes in Figure 1 show the solutions as determined in the USGS catalog. The magnitudes of the two associated earthquakes in the northern part of Illinois are M_w 3.8 and 4.2 and occurred at 11 and 7 km depth. The two large earthquakes indicated by source mechanisms in the southern part of the state occurred at a depths of 14 and 18 km, and are a magnitude 5.2 mainshock follow by a magnitude 4.0 aftershock. An analysis of different types of stress measurements in the Illinois Basin by Lahann *et al.* (2017) shows that the azimuth of the maximum horizontal stress has a fairly constant northeast azimuth for northern and central Illinois, consistent with the orientations of the strike-slip failure. The source mechanisms determined from induced seismicity in the Decatur area (marked by the small box labeled IBDP in Fig. 1) also show strike-slip failure with similar failure plane orientations, discussed in this article and also reported by Langet *et al.* (2020).

The injection target of the IBDP is the lower part of the Cambrian Mt. Simon sandstone, an extensive formation that underlies much of the Midwestern United States, which is also used regionally for seasonal geological storage of natural gas. Geological site characterization of the IBDP is based on examination of more than 250 m of whole core, well logs, 2D and 3D seismic, and a range of core and sample tests and analyses (Freiburg *et al.*, 2014). The maximum reservoir thickness of approximately 790 m occurs near the injection site, and the lithostratigraphy of the Mt. Simon is divided into lower, middle, and upper sections. Freiburg *et al.* (2014) identified fluvial braided stream, floodplain, and alluvial plain deposits, eolian sheet sand, dune and interdune deposits, and shallow marine deposits. Thin (1.5–3 m thick) discontinuous lenses of low permeability mudstones occur throughout the Mt. Simon that act as baffles, partially restricting vertical fluid flow within the reservoir (Couëslan, Smith, *et al.*, 2014). In the CCS1 well, CO_2 was injected into the lower Mt. Simon sandstone in which the highest porosity occurs, averaging 22%, and average permeability is 200 mD ranging up to 1000 mD (Leetaru and Freiburg, 2014). Current injection in the CCS2 well is at a depth about 46 m shallower than the CCS1 injection zone (Fig. 2) but still within the lower Mt. Simon. The permeability in the perforation zone averages about 250 mD but can be as high as 1066 mD (Freiburg *et al.*, 2014). The average porosity in the interval is 28%. The overlying Eau Claire formation is a 150 m thick, very low permeability package that hydraulically isolates the Mt. Simon from overlying strata (Palkovic, 2015). The lower 70 m of the Eau Claire is a shale that serves as a highly effective seal to vertical fluid movement. The base of the Mt. Simon lies nonconformably on top of a series of strata informally designated by the ISGS as the Argenta formation, previously identified as the pre-Mt. Simon, to distinguish it from both the Precambrian basement and the Mt. Simon sandstone (Freiburg *et al.*, 2014). This underlying unit consists of compacted sandstones and pebble conglomerates with clay cements and angular clasts of basement rock. Average porosity of this unit is 9% and permeability averages around 2 mD (Leetaru and Freiburg, 2014). The Argenta formation base is a sharp, nonconformable contact with the Precambrian crystalline basement.

Reservoir characterization

Pre-existing regional 2D seismic data were the primary source of structural information for predrill site characterization. In 2007, two additional 2D seismic profiles were acquired along

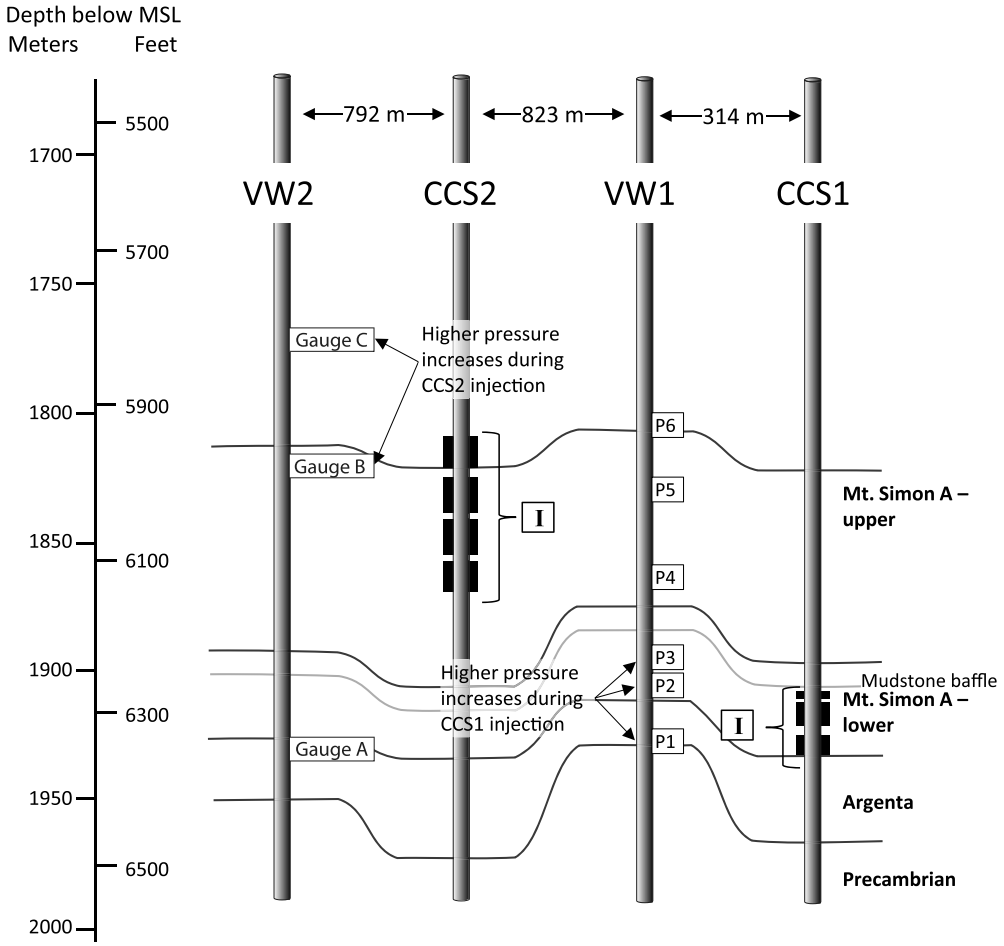

Figure 2. Schematic view of the two injection and two monitoring wells. The black bars (labeled I) indicate the perforation zones for CO_2. The labeled boxes next to verification wells (VW1 and VW2) show the ports or gauges for pressure measurements in the monitoring wells. For details of the completions in CCS1 and VW1, see figure 19.5 in Bauer *et al.* (2019). The gray line indicates the approximate location of a mudstone baffle below which pressure increases were much greater in CCS1 during injection. Pressure increases above the mudstone are much greater during CCS2 injection, which is interpreted to have restricted vertical migration of injected CO_2 and fluid pressure. MSL, mean sea level.

east–west and north–south roads that pass the ADM plant and injection site. After a positive preliminary assessment of the area, four additional 2D seismic data lines were acquired at the site in November 2009 and February 2010 to obtain additional geological detail and supplement predrill planning (Bauer *et al.*, 2019).

Three separate 3D seismic acquisition efforts were carried out. The first in 2010 was designed for detailed site characterization over the anticipated CO_2 plume area, and the second acquisition in 2011 extended this survey. Together these surveys served as the baseline for time-lapse monitoring work. The third survey, conducted in 2015, took place after completion of CO_2 injection in CCS1. The main processing objectives for the 2010 and 2011 3D seismic surveys focused on site characterization, with processing flows designed for merging the 2010 and 2011 survey, seismic data inversion, and structural interpretation. The noise level at the site is high, and applying a series of premigration filters improved the image quality. Another objective for the seismic imaging was identification of faults in the subsurface zone of interest. Figure 3 shows the components of the seismic acquisition at Decatur, including the area of the 3D survey and two of the 2D reflection lines. The 3D reflection seismic data acquired in 2015 were reprocessed in 2019, using processing workflows, with this purpose in mind.

The improvement in seismic image quality from the 2019 reprocessing was obtained by carefully defining the wavelets defining the reflectors of the major horizons in the seismic data. The precise wavelet determination calibrated with the wellbore velocity information increased the definition of the reflectors (Fig. 4). The acoustic impedance from the well logs was then used to produce an acoustic impedance volume from the active seismic data. Data input to the porosity volume included the seismic reflection volume, the acoustic impedance inversion volume, and the effective porosity logs. A multivariate statistical approach was run using different scenarios to select the best possible combination of seismic attributes to match effective porosity logs, and the parameters derived from the best multivariate model were used as input to a probabilistic neural network analysis to derive predicted porosity. The neural network analysis produced a relationship of actual porosity to predicted porosity values with a correlation coefficient of 0.97.

The differences in average porosity for different units are well imaged in the porosity volume (Fig. 5). A stark porosity contrast exists at the base of the high-porosity Mt. Simon sandstone at the contact with the Argenta formation. The increased resolution reprocessing combined with the neural network predicted porosity enhanced porosity contrasts that were difficult to distinguish in original processed volume. The seismic inversion associated the lowest porosity with

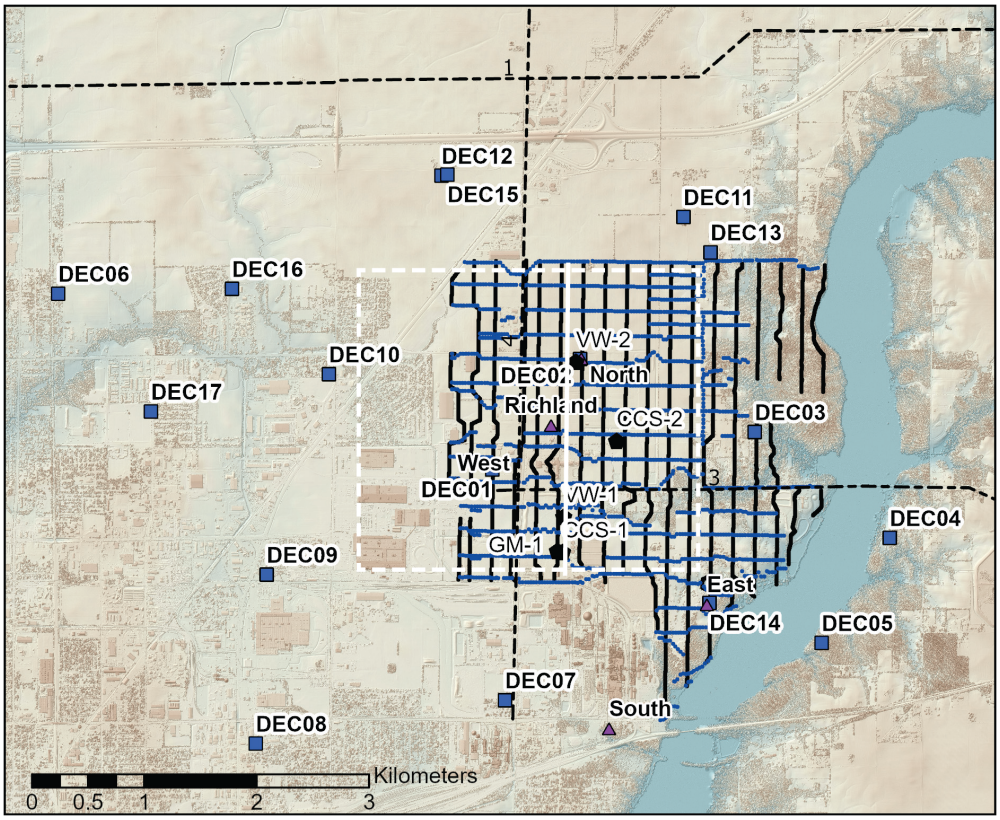

Figure 3. Map of the active and passive seismic acquisition configurations for the IBDP. This location is shown as the black square in Figure 1. The small (~10 km^2) 3D seismic footprint covers Archer Daniels Midland property, which comprises 40% of the area located in the southern part of the survey area, and the rest is land owned by 160 individual owners used predominantly for farming. The north–south and east–west dotted black lines crossing the 3D acquisition survey points are the locations of two of the 2D seismic lines acquired through the site. The dark squares are USGS seismometer locations and the dark triangles are locations of ISGS seismometers. The two injection wells, CCS1 and CCS2, and two monitoring wells, VW1 and VW2, are indicated by the black symbols. The solid white north–south line shows the approximate location of the seismic lines in Figures 4 and 5. Richland Community College is a few hundred feet to the north of the CCS2 well location. The white dashed rectangle is the boundary of the subsurface model shown in Figure 8. The color version of this figure is available only in the electronic edition.

the Precambrian crystalline basement rocks, and a second very distinct porosity boundary is now visible beneath the top of the Argenta. Only the top 30 m of the basement was penetrated in the CCS1 well, in which intact core recovery was difficult, and the resistivity image log analysis indicates that it is highly fractured.

The MOVE 2019.1 structural geology and analysis software suite was used to visualize the relationship of the fault geometry to the spatial distribution of microseismic clusters and to create dip planes from the source mechanisms (Fig. 6). The maximum horizontal stress orientation determined from wells at the site is 68° azimuth (Figs. 1 and 6). Microseismic events in the basement were the initiation point of one of the earliest clusters near the CCS1 injection well, indicating early reservoir connection to the basement. Goertz-Allmann *et al.* (2017), working on a microseismic cluster north of this high, proposed a subseismic basement connected fault-enabling fluid and pressure migration into the basement; a fault fluid pathway that was also suggested by Couëslan *et al.* (2013) and Kaven *et al.* (2014).

The much lower porosity and permeability of the Argenta formation may enable it to act as a "bottom seal" between the base of the Mt. Simon and the Precambrian basement, wherever it is present. The reflectors interpreted as top basement and top Argenta are very close in some places (Figs. 3 and 4), indicating areas primarily on the topographic highs where the Argenta may be missing either due to erosion or nondeposition. The updated porosity inversion supports an additional contributing factor influencing pressure migration, which is that the Argenta formation may not be thick enough everywhere to effectively inhibit downward flow into the basement.

Passive seismic monitoring

The primary elements of the passive seismic monitoring array are in the CCS1 well, with an access for repeat geophysical logging, and comprises a two-level array of four-component geophones in tetrahedral configuration (Bauer *et al.*, 2019). The adjacent GM1 well hosts a 31-level array of three-component geophones in orthogonal configuration for repeat vertical seismic profile data acquisition, which enabled it also to serve as a vital component of the passive seismic monitoring network. Data were also collected from a five-level array of three-component geophones that were temporarily installed in a monitoring verification well (VW2) to be used for the IL-ICCS project. All of the elements of the monitoring array and of the active seismic acquisition are described in detail in Bauer *et al.* (2019), and the reader is referred to that publication for additional information.

A local network of surface and shallow borehole seismometers was installed by the USGS about 18 months after injection

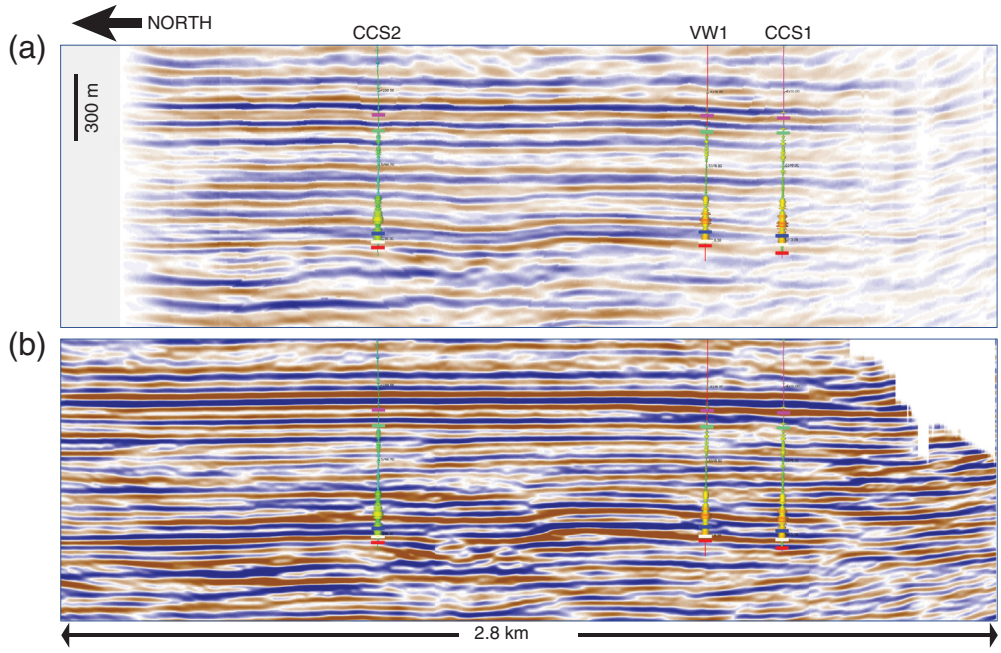

Figure 4. (a) Original processed seismic and (b) reprocessed seismic comparison of the same cross section through the 3D volume, showing greater detail and higher resolution imaging of features that indicate faulting. The CCS1, VW1, and CCS2 wells are projected onto the seismic; all three wells are less than 32 m from the cross section, projected orthogonally on to the cross section. Depth range of the cross section is from −1100 to −2260 m. The color version of this figure is available only in the electronic edition.

commenced (Kaven *et al.*, 2015). The ISGS also installed five additional surface seismometers, and the two installations comprise a local network of 22 seismometers on or near surface above the IBDP injection site with an aperture of about 10 km centered on the injection and monitoring wells (Fig. 5).

One month after CO_2 injection commenced, in December 2011, two microseismic events were detected, followed by 14 locatable events in January 2012. A large spike in microseismic activity occurred in February 2012, when over 500 locatable events were recorded. Microseismicity continued to occur at mostly lower but variable rates per month for the duration of the injection. After the CCS1 well was shut, seismic activity was observed to decline for a period of approximately six months, reaching a level of activity of between 2 and 15 events per month which persisted for the remaining 22 months of shut in prior to the start of injection in the CCS2 well. The seismicity rate showed negligible increase after injection in the CCS2 well, which to date has averaged 0.5 Mt/yr injection for its 2.8 yrs of operation.

The USGS reported 150 located events from July 2013 to February 2015 in Kaven *et al.* (2015), representing only a small subset of the events located by the downhole sensors, but the azimuthal coverage of the surface stations provided important information about the failure mechanisms for improved understanding of the reservoir stress and geomechanical response.

The waveforms used for analysis in this study are a subset of 50 events from the USGS catalog (Kaven *et al.*, 2015) using data from the USGS network combined with the five seismometers at the site operated by the ISGS. Source mechanisms were determined for the 50 selected events and included events from multiple clusters chosen for interpretation based on data signal-to-noise ratio to explore, if failure plane orientations correspond to the orientation trends of the microseismicity clusters.

Post-CCS1 injection monitoring

The number of detected events per month does not show a significant increase, after injection begins in the CCS2 well (Fig. 7b). The original injection plan for CCS1 and CCS2 wells was designed to investigate the interaction between two wells with simultaneous injection into the same reservoir zone and to also inject into a shallower interval in the CCS2 well. Permitting delays allowed time to reassess the geologic controls on the microseismicity. The decision was made to raise the bottom of the injection in CCS2 to a higher interval above a mudstone baffle, which constrained CCS1 pressure increases and microseismicity from progressing upward.

The presence of mudstone baffles is supported by pressure data collected from the subsurface gauges illustrated in Figure 2. The VW1 well is in an area where many microseismic clusters occur, but there is significantly less seismicity in the area immediately adjacent to the CCS1 well (Fig. 6). The CCS2 injection pressure changes observed in the VW2 well from gauges in zones above the mudstone baffle are significantly larger than the pressures observed during the CCS1 injection (Fig. 2). The pressure increase above the mudstone baffle was up to 6.7% higher than the original formation pressure. During CCS1 injection, the pressure increased in this area by only as high as 0.75%. In comparison, below the mudstone baffle, the pressure increase during CCS1 injection was 5.4%, and during CCS2 injection, pressure increase in the same area is only 2.2%. These pressure relationships suggest upward restriction of pressure migration during CCS1 injection, leading to induced seismicity in the basement to the north of the CCS1 well where the Argenta formation is thin or absent,

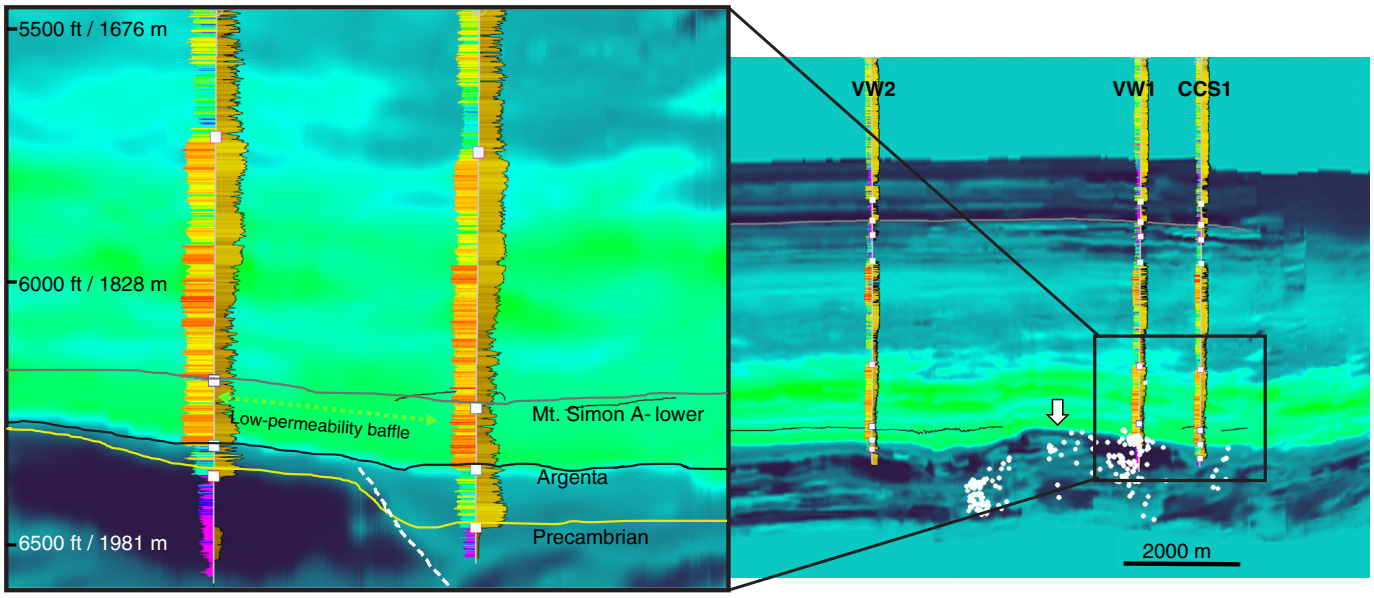

Figure 5. Porosity inversion of the same volume slice shown in Figure 3, showing distinctly in which the rock property inversion indicates zones of high and low porosity. The darker hues in the lower middle part of the section indicate the high-porosity zones of the Mt. Simon. A white arrow near the middle lower part of the image points to a basement high in which Argenta may be thin to absent. The enlarged detail (left) around the bottom of the CCS1 and VW1 wells show where the top of the Mt. Simon A reservoir target zone is interpreted. The lighter color below the base of the Mt. Simon is the lower porosity Argenta, where the neural network predicted porosity of the reprocessed 3D seismic volume now distinguishes the Argenta porosity from the Precambrian basement porosity (darker gray below the Argenta). The logs shown on the left side of the well are colored by permeability, ranging from about 200 to 1000 mD, and the right side log indicates gamma-ray values showing darker colors for more shaley layers with values for the displayed intervals ranging from about 50 to 150 gAPI. The lower black line marks the top of the crystalline basement, showing that Argenta is thin or missing on the paleotopographic high to the north of the VW1 well. The dashed line indicates the location of a fault interpreted between VW1 and CCS1, where there Argenta porosity abruptly thickens. Section is displayed with 2× vertical exaggeration. The white line on the map in Figure 2 indicates the location of this cross section. Wells and microseismic events are projected onto the section from up to 70 m. The color version of this figure is available only in the electronic edition.

and downward restriction during CCS2 injection, in which the baffle may have restricted pressure communication to the basement.

FAULT CHARACTERIZATION

Features that have been interpreted as faults and converted to modeled surfaces are shown in Figure 8. The faults are displayed in the MOVE 2019 structural analysis software truncated close to the top of the Precambrian basement, which is shown partially transparent, so that the events and the fault dips remain visible. The fault lengths range from approximately 250 to 1000 m, although some may be composed of multiple intersecting fault planes or intersecting smaller faults. The vertical displacement of most of the faults is at or below seismic resolution, but their presence is interpreted by the disruption in the character of the seismic reflector at their location.

Orientations from the source mechanisms were compared to the fault planes from the reflection seismic. Using passive seismic data from more than one acquisition array type and combining with active seismic data to make an integrated data interpretation require the use of a consistent velocity model for all the different data sources, and much of the data have been processed and interpreted separately. Seismometers and geophones have different instrument responses; corrections can be applied, so that it is generally not a problem for the model. Using the same frequency range for both active and passive data eliminates the need to consider frequency-dependent seismic velocities. Even with the appropriate corrections for instrument response and consistent velocity model, the locations and magnitudes of the surface seismometer data are not the same as those associated with the events acquired from the downhole monitoring. Such mismatch of events is sometimes observed in datasets in which both surface and downhole data were acquired (Eisner *et al.*, 2010; Peyret *et al.*, 2012) and is related to both the general velocity model characteristics and the waveform propagation effects for a travel path that is primarily horizontal versus vertical. The event relocation effort using the combined sensors for a 3D detection array described in Langet *et al.* (2020) was focused on cluster 18 and significantly reduced the event location error, collapsing most locations into the shape of a well-defined east–west plane. The alternate approach used in this study does not lead to reduction in location error but integrates event failure plane information from origin time matched events using information unique to each acquisition method to develop an integrated geological interpretation.

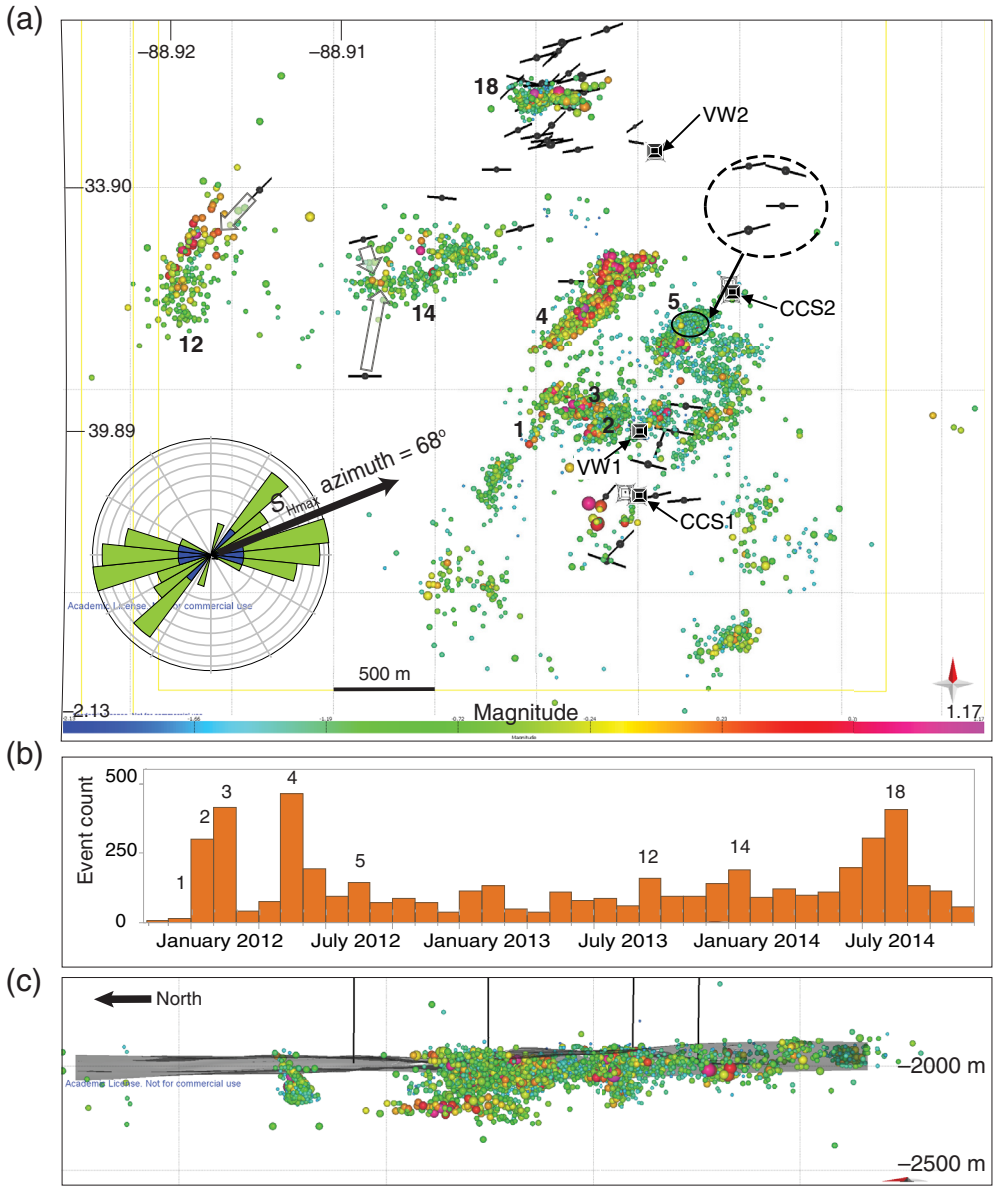

Figure 6. (a) Map of induced seismicity during injection in the CCS1 well. Dots are epicenter locations of downhole sensor-detected events. The strike of source mechanism failure planes is indicated by the black lines (sized by relative magnitude) centered on a black dot located at the epicenter of events located using the USGS and ISGS seismometer stations and without using additional constraints from downhole data. The rose diagram shows the (bidirectional) strike azimuths of the source mechanism failure planes with the azimuth of the maximum horizontal stress. The dark portion of the petals indicate strikes associated with dips less than 50°. (b) The histogram shows the frequency of events per month for the entire injection period of CCS1. The numbers next to some of the clusters indicate their relative appearance over time, with the same number over the histogram bin for the month the cluster appeared. (c) Depth section view of microseismicity from the west showing location of events relative to the top of the Precambrian basement. The color version of this figure is available only in the electronic edition.

The subset of 50 events that were relocated using the USGS and ISGS surface seismometers is shown as black spheres centered on a line parallel to the strike of the failure plane in Figure 6. The rose diagram in Figure 6 shows the strike distribution of the likely failure planes orientated within 30° of the maximum horizontal stress determined from the borehole data, and majority of these have dips ranging from 50° to 90°. Faults interpreted from the active seismic volume include some north–south and northwest–southeast orientations, which would not be likely to slip in the current stress field, and none of the clusters display these trends. One surface array-located event corresponds by time to an event near the middle of cluster 12 and has a failure plane strike parallel to the northeast trend of that cluster. Two surface events correspond to events in cluster 14, and they also strike east–west, parallel to that cluster. Cluster 18, the cluster analyzed in Langet *et al.* (2020), has an east–west trend. Although the failure planes from this study strike primarily parallel to the cluster elongation trend, they are spread significantly to the north and south of that cluster, indicating large relative mislocation. The largest relative mislocation is for the four surface-located events inside the dashed circle in Figure 6 that correspond to downhole locations in cluster 5. These events have unique waveforms, which increased their location uncertainty due to higher picking uncertainty and velocity model uncertainty. Their failure plane orientations also do not strike parallel to the trend of cluster 5, suggesting that the clusters could be associated with multiple faults and/or fault splays. The east–west-faulting component interpreted in the active seismic data is clearly seen in the northernmost event cluster 18 and is present in some of the other clusters as a subtrend in the microseismicity.

The general spread of microseismic activity toward the north of the CCS1 well and west and north of the CCS2 well suggests that pressure migrated in a direction either at a high

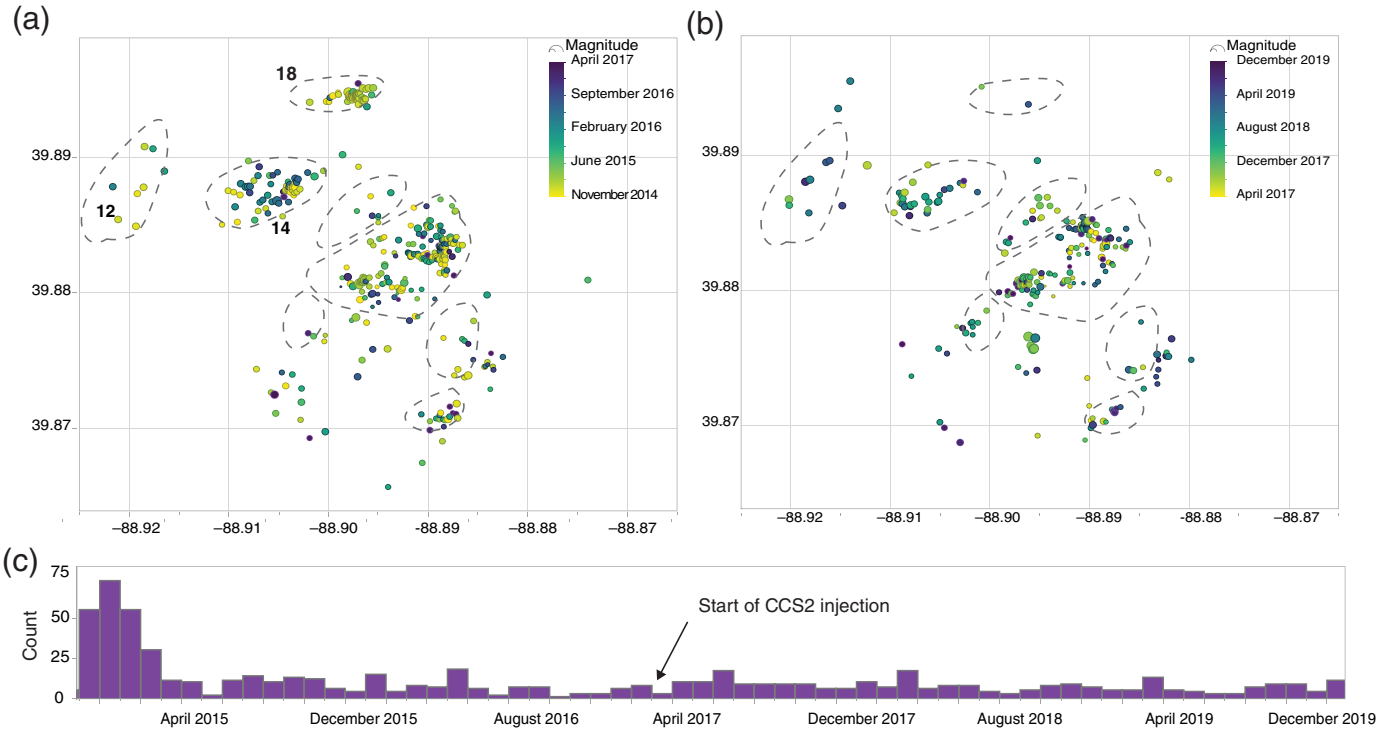

Figure 7. (a) Maps of microseismicity detected by downhole sensors during the period in which no CO_2 injection took place and (b) after injection started in the CCS2 well. The dashed loupe indicates approximate areas and locations of some of the clusters, with three clusters labeled for comparison to their locations in Figure 6, showing that postinjection events occur within the previously established clusters. (c) Histogram of number of events detected by month starting with the noninjection period and including CCS2 injection through the end of December 2019. A negligible increase in seismicity occurs after a 1.7-fold increase in injection rate in the CCS2 well. The color version of this figure is available only in the electronic edition.

angle to the fault failure planes, open fractures of other orientations connect the fault planes imaged by microseismicity, stress transmission was a factor determining locations and extent of induced seismicity, or there are fewer critically oriented fault zones in different areas. Because of the difficulty imaging potentially seismogenic faults, modeling possible fault and fracture networks based on estimates of fault sizes in the population could be done to investigate the degree of fault connectivity and provide input to reservoir simulation models. A methodology for constraining fault sizes is discussed in the following sections.

Fault-size estimates

The fault interpretations from the 3D reflection seismic volume provide coarse constraints for a preliminary estimate of the size range of faults in the subsurface at IBDP that were reactivated by CO_2 injection. The trace of the longest interpreted fault length, shown in Figure 7, is approximately 1.2 km, with the faults as small as 0.25 km mapped. These trace lengths likely represent a minimum length, as displacement near the fault tips is generally below seismic resolution. The sinuous character of most of the interpreted faults suggests that they are composed of multiple fault splays. Estimates of fault area, including fault tips, have been published by workers in the oil and gas industry, because of the importance of fault displacement for estimating juxtaposition of sealing rocks and reservoir rock for reservoir formation (Rotevatn and Fossen, 2011). Given the uncertainty in the source-scaling relationships and with fault interpretation geometries, we assume the mapped fault trace to be a reasonable constraint for calculating fault-plane size to compare to interpreted fault-plane size. Using the relationship given in equation (1), a fault-plane size can be calculated from the rock rigidity, the average slip on the plane, and the moment magnitude:

$$M = \mu A D, \tag{1}$$

in which M is the moment, μ is the shear modulus of the rock (Pa), A is the fracture surface area (in meters), and D is the average displacement length (in meters). The shear modulus used in the calculation is 2.34×10^9 MPa, measured experimentally on rock samples recovered from the top of the Precambrian. In the case of large earthquakes with surface rupture, displacement can be measured directly and further constrained by locations of aftershocks on the main fault plane. In the case of earthquakes without measurable surface rupture, as is the case for all induced events at the IBDP, neither the length of a seismogenic fault or the average slip can

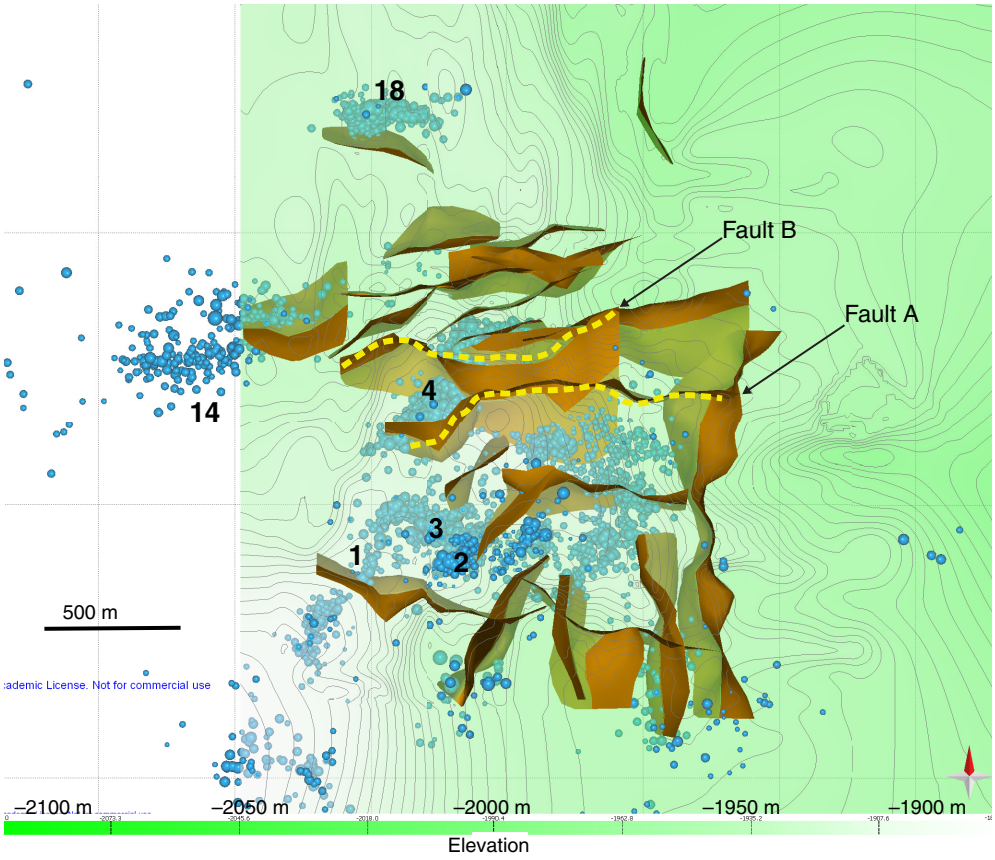

Figure 8. Microseismicity displayed with the interpreted top of the Precambrian surface displayed with transparency, so that events below the surface are visible. Darker gray colors on the surface are deeper, and relative highs are lighter in color. The faults interpreted from the 3D seismic volume are shown as mostly sinuous 3D surfaces. The longest interpreted east–west fault is marked by a dashed line. Some of the microseismicity clusters are labeled in black; the northeast-trending cluster 4 is cut by multiple faults with east–west strike. Note that many of the events fall outside of the 3D seismic coverage, and the fault nearest to cluster 14 has strike similar to the orientation trend of that cluster, but that fault is likely truncated because it is outside of the seismic volume. A loose correlation can be seen in which some fault trends (or parts of faults) parallel to microseismicity. The white dashed rectangle in Figure 3 indicates the extent of the view in the figure. The color version of this figure is available only in the electronic edition.

be measured. Published slip length relationships have been established for large earthquakes (Wells and Coppersmith, 1994; Martin Mai and Beroza, 2000; Shaw and Scholz, 2001; Thingbaijam *et al.*, 2017). Studies of microseismicity in mines indicate that the frequency–magnitude relationships are valid to very small events (Abercrombie, 1995; Kwiatek *et al.*, 2011). Fewer studies are available that address whether fault plane–slip-distance relationships also hold for events in the microseismicity range. McGarr and Fletcher (2003) investigated whether rupture processes are different for small and large earthquakes and discovered that the maximum slips to seismic moment relationships inferred for large earthquakes are consistent with those measured from stick-slip laboratory experiments. We use source-scaling relationships derived by McGarr and Fletcher (2003) and Thingbaijam *et al.* (2017) to estimate failure plane sizes of the IBDP events. The McGarr and Fletcher (2003) relationship is given in equation (2), as

$$D = 10^{-5.83} \times (M_0)^{1/3}, \quad (2)$$

in which D is the displacement distance and M_0 is the seismic moment, calculated using the relationship given in Hanks and Kanamori (1979):

$$\log M_0 = 1.5M_w + 16.1. \quad (3)$$

The microseismic energy of the IBDP-induced events is calculated as M_w. Thingbaijam *et al.* (2017) determined an empirical source-scaling relationship by examining different types of faulting. The scaling relationship from their analysis, using the strike-slip relationship, is shown in equation (3):

$$D = 10^{-4.032+0.558\times M_w}. \quad (4)$$

The resulting fracture and fault-plane sizes are shown in Figure 9. The size is given by source radius, assuming a circular slip patch, in which twice the radius is used as a proxy for the maximum length of the fault-slip patch in the reservoir. The McGarr and Fletcher (2003) relationship generates failure planes that have shear-plane areas less than 2 m diameter to a maximum length associated with the largest magnitude event of less than 80 m. The relationship of Thingbaijam *et al.* (2017) calculates much larger slip planes, from 8 m to more than 120 m in diameter for the magnitude range of microseismicity detected at this site. In each case, the calculated slip patch radius is much smaller than the any half-length of mapped fault trace lengths in the reservoir.

The shapes of many of the mapped faults suggest that they are composed of multiple interconnected faults with different strike. The longest individual fault trace (fault A in Fig. 8) is sinuous, but mostly east–west in orientation, nearly intersecting microseismicity cluster 4 at an angle approximately 30° to its elongation direction. This fault bends to strike nearly parallel to the trend of cluster 4, a few tens of meters before it intersects the cluster, supporting an interpretation of more

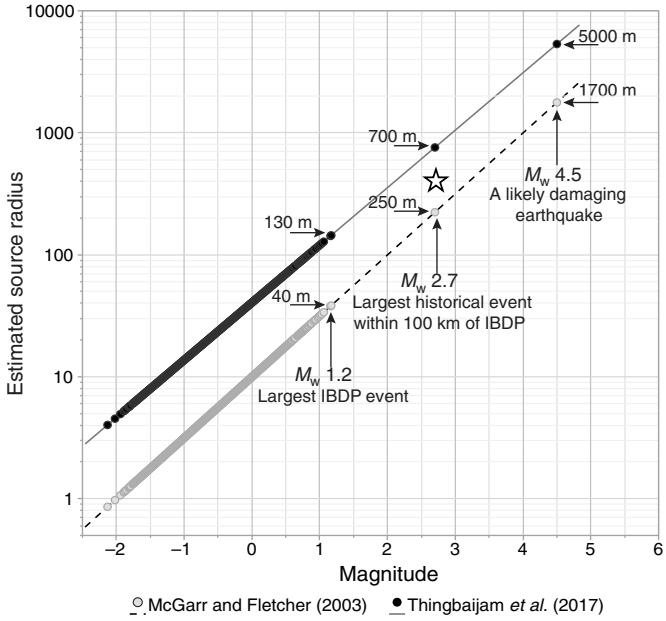

Figure 9. Slip-distance relationship to magnitude using McGarr and Fletcher (2003) and Thingbaijam *et al.* (2017), calculated using magnitudes of all downhole events and the 50 events acquired from the surface seismometer stations. The gray dots show the source radius calculated using McGarr and Fletcher (2003), which are smaller than the source radius calculated using Thingbaijam *et al.* (2017) shown by the black dots. Three source radii that are significant to the IBDP are indicated on the plot for both relationships: the source radius for the largest event detected during injection (M_w 1.2), the source radius for the largest historical earthquake within 100 km of Decatur (M_w 2.7), and the source radius of a potentially damaging earthquake (M_w 4.5). The star in the middle of the two lines represents a fault-size estimates in which the source radius is approximately equal to the size of the largest faults interpreted in the reflection seismic data.

than one fault. Cluster 4 developed prior to installation of the surface seismometers, so data for source mechanism inversion of these events were not acquired. The shape of cluster 4 also shows a rather sharp east–west boundary on its northern end, suggesting a splay or intersection with a fault in that orientation, possibly the large interpreted fault (B) that intersects the northern end of the cluster. Clusters 14 and 18 each have a fault interpreted nearby with a similar orientation, but the locations are not exactly coincident, which could be due to stronger influence of horizontal velocity differences on downhole-detected events.

An important outcome from the microseismic monitoring is the information that can contribute to assessment of risk related to induced seismicity (Skoumal *et al.*, 2015; Barbour *et al.*, 2017). Identifying the locations of faults with the potential to cause damaging earthquakes can sometimes be done prior to activities that perturb the subsurface stress state when high resolution, good-quality seismic reflection data are available, and any strike-slip faults have enough vertical offset to be detected. Structural interpretations from well data can also be used to identify faults, but they are not as useful when there are few wells or the well spacing is sparse or features are nearly vertical and paralleling the borehole. The microseismic data serve to fill the gap between the two scales and can validate interpretations on seismic reflection data or provide information between structural well data.

DISCUSSION

A question that is important to answer when analyzing induced seismicity is "how big could the events be?" In the IBDP, no felt seismicity occurred with injection, and changing the injection interval greatly lowered the number of detected microseismic events. Using the assumption that the size of the faults in an area is an important control on the potential size of induced events, the fault-size estimates could potentially be used to provide an answer to that question (e.g., Magnani *et al.*, 2017; Scales *et al.*, 2017). Instances of fluid injection associated with felt seismicity are also associated with faults in the subsurface that are much larger than the faults identified beneath the Decatur site. Although the sharp increase of induced seismicity from wastewater injection has led to a sharp increase in the amount of information in the peer-reviewed literature about subsurface faulting in Oklahoma, indications of the size and extent of these faults have been in the oil and gas industry literature for decades. Benoit (1958) produced maps of the base of Pennsylvanian rocks in Oklahoma and Canadian Counties for an area of approximately 150 km^2 that is located less than 20 km north of Oklahoma City. Interpreted fault lengths of 5 km or more were mapped in the study area using information from the numerous, nearly regularly spaced wells. By the 1970s, oil geologists understood the importance of faults as an oil-trapping mechanism, and careful mapping faults in the subsurface were often used to define reservoir provinces and aid in exploration (Hollrah, 1979). The mapped trace length of a fault only provides part of the fault-size information, and the amount of mappable displacement on a fault can also be used to estimate the 2D size of the fault plane. The subsurface mapping of a 5 km long fault trace by Benoit (1958), for example, shows at least 100 m maximum displacement. It is not unreasonable to expect faults with displacement and length in this range to be deep enough to penetrate the crystalline basement (Dawers *et al.*, 1993; Gudmundsson *et al.*, 2013).

Fault maps of Oklahoma updated with industry-provided data show fault traces hundreds of kilometers long (Holloway *et al.*, 2016). Many of the largest faults are not oriented optimally for slip in the current stress regime, but in the assessment by Walsh and Zoback (2016), the relatively small portions of the faults they determined were likely to slip in response to injection are 10–15 km in length. Mapping of events using a relocated template-matching catalog changed the locations of seismic events, so that they align very nicely with the more east–west trends of faults that are likely to slip, many of which were also previously identified in the industry

literature but not generally publicly available. Wastewater injection in Oklahoma and in other oil field operations has taken place since the 1960s, but the growth of hydraulic fracture stimulation in unconventional oil and gas production, and the increased production in conventional resources with very large produced water content during the late 2000s significantly increased the volume of wastewater needing to be disposed (Scanlon *et al.*, 2019). The resulting increase in felt seismicity suggests that although oil and gas operators were aware of significant faulting in the subsurface, waste disposal operators may have had insufficient knowledge of hydraulic connectivity with the basement or of the reservoir geomechanics and the impact on the reservoir from the introduction of much larger fluid volumes at high injection rates.

When considering historical felt seismicity in the Illinois basin, natural earthquakes larger than magnitude 3 have not been reported within approximately 100 km from IBDP site. In comparison, at least one historical earthquake larger than M_w 5 was recorded in 1952 near El Reno, Oklahoma, near areas where wastewater injection occurs, and reports of other felt earthquakes were made as early as 1918 (Miller, 1956).

The relationships of moment magnitude to slip area of McGarr and Fletcher (2003) and Thingbaijam *et al.* (2017) estimate the slip patch size for the largest induced seismic event at the IBDP site (M_w 1.2) could have a radius of 40–130 m. The largest clusters of induced events span a distance of about 800 m, potentially indicating the length of a reactivated fault. Slip on the entire surface of a fault of this size could correlate with M_w 2.7, similar to the largest nearby historical earthquakes in Illinois. The Dallas–Fort Worth Airport fault has a mapped trace length of 35 km, with a relatively large displacement across the fault of 300 m (Hennings *et al.*, 2019). A displacement of 300 m would be easily identified in reflection seismic data. The displacements across the largest fault interpreted in the IBDP seismic volume are about 10 m and the trace length approximately 1 km, consistent with the observed microseismicity.

The depth of the induced seismicity confirms that some of these faults penetrate the basement where it is more difficult to identify horizon offsets in the reflection seismic. It is possible that significant fault displacement occurred in the Precambrian rocks prior to deposition of the Argenta formation and was subsequently eroded, so that the fault displacement visible in the overlying sediments is significantly smaller than that of the basement. However, a strong reflector in the seismic reflection data has been imaged in the 3D volume about 1700 m below the top of the Precambrian basement. This reflector is also imaged in the 2D seismic lines acquired across the Decatur site and has been interpreted as a mafic igneous sill that corresponds to a nearly 30 km wide magnetic anomaly (McBride *et al.*, 2016). Within the 3D volume, a few disruptions of this reflector that could be interpreted as small displacement faults are visible, and in some of the 2D seismic lines imaging more marginal areas of the basin, approximately 30 km west of the IBDP site, larger offsets have been interpreted as possible faults (Freiburg *et al.*, 2020). McBride *et al.* (2017) proposed that the sill could have caused the development of damage zones with fractures of varying orientations in the overlying rocks from processes related to intrusion.

Studies of hydraulic fracture monitoring in oil and gas may provide some clues regarding reservoir properties that could influence induced event energy. Hydraulic fracturing microseismic monitoring in the Williston Basin Bakken Formation detects very low amplitude events (Williams-Stroud *et al.*, 2013; Dohmen *et al.*, 2017), and there is also no change in regional seismicity in North Dakota associated with the substantial increases in wastewater disposal from oil and gas production (van der Baan and Calixto, 2017). Wastewater injection activities may be more correlative with CO_2 injection in which a product is injected for storage than with hydraulic fracturing where the fluid is pumped back out of the well. Earthquake data recorded by the USArray between 2008 and 2011 detected very few earthquakes near injection wells in the Williston basin (Frohlich *et al.*, 2015). The Williston basin has structural similarities with the Illinois basin, as both are shallow depressions with an apparent lack of significant large displacement faulting near the injection locations. Frohlich *et al.* (2015) did not offer a conclusion to explain why the induced seismicity rates in the Williston basin were also lower than in Oklahoma but speculated that some of the injection wells in Oklahoma had higher injection rates. In comparison, the average CO_2 injection rates of 1123 m^3/day for CCS1 and 1951 m^3/day for CCS2 are in the range and in many cases far greater than rates associated with induced felt and damaging earthquakes from wastewater injection. Frohlich (2012), for the Barnett Shale, found induced seismicity associated with eight wells with maximum monthly injection rates exceeding 14,000 m^3/month (800 m^3/day), and these rates were maintained for a year or more prior to the onset of earthquake activity. In other areas of the Barnett Shale, there were 100 similar wells, with rates exceeding this and no nearby earthquakes. Horton (2012) reported eight wells with peak rates ranging from 631 to 2021 m^3/day along nearby faults that induced earthquakes. A general analysis by (Weingarten *et al.*, 2015) attributed injection rates greater than 1540 m^3/day, with a greater than expected likelihood of association with earthquakes, as shown by map view proximity to each other. In the Michigan Basin, 30 wells operate at maximum injection rates greater than 1026 m^3/day with no seismicity (Weingarten *et al.*, 2015, their Supplementary Materials). The lack of seismicity detected could be explained by a lack of monitoring, but in Illinois, an industrial complex has injected waste since 1966, with rates as high as 2600 m^3/day, with a massive total of 75 million cubic meters injected without any felt or networked detected seismicity, which would likely have been detected during the period of

coverage by the USArray. Finally, chemical effects and the nature of the injection fluid, brine as opposed to supercritical CO_2, may play an important role in reservoir response and need to be better understood; but they are beyond the scope of this article.

During the In Salah CO_2 project, injection was stopped because of surface elevation changes from slip on faults, which was directly observed using Interferometric Synthetic Aperture Radar (White *et al.*, 2014). In addition, a large number of microseismic events were detected in different clusters at that project, which could be contributed to periods of injection pressures above the fracture pressure and triggered seismicity on pre-existing faults. Detailed locations and the detection of more of the smallest events were not possible at In Salah due to an absence of deep sensors, in comparison to the IBDP and IL-ICCS project (Goertz-Allmann *et al.*, 2014).

CONCLUSIONS

Fault size and reservoir character are important factors contributing to the potential for felt seismicity, but other reservoir properties may also influence the detection of seismic energy. Although felt seismicity has not been reported from CO_2 injection activities, projects may not have benefitted from sufficient instrumentation. In these and other situations, induced microseismicity could go completely undetected, if appropriate instrumentation is not installed. The importance of the acquisition network geometry and coverage should not be underestimated, as the results of other fluid injection experiments have shown. A dense surface network or multiple downhole strings, or both, may be the minimum geometry required to effectively characterize microseismic events. The ability to compare separate results from different acquisition configurations provides useful information for future monitoring array designs that could be applied to other projects in which acquisition is limited to one method.

These two companion projects, IBDP and IL-ICCS, provide important information about the impact of injection-well placement with respect to the subsurface geology. Significant induced seismicity resulted from injection in the first well, in which the injection zone was near the base of the Mt. Simon, and is also located near an area where the potential "bottom seal," the Argenta formation could be absent. Migration of fluid pressure into the basement rocks may have been facilitated by this combination of location, stratigraphy, and rock properties. The scarce microseismicity currently being detected during injection in the second well could be explained by the presence of mudstone baffles below the injection interval, which likely inhibited vertical flow and thus led to connection with faults in the basement. In addition, core and image log observations of the Mt. Simon indicate very little fracturing in the rock. The paucity of fractures combined with the very continuous nature of seismic reflectors in the 3D volume supports an interpretation that the Mt. Simon does not contain faulting in the shallow zones that are large enough to penetrate the basement, and faults could not be interpreted above the middle Mt. Simon zone. The mudstone baffle may also have played a role in early migration of fluid pressure down into the basement by restricting upward migration shallower into the Mt. Simon. Although the baffles are discontinuous, they appear to be common, and the high permeability and porosity zones in the Mt. Simon sandstone can easily accommodate horizontal fluid and pressure migration.

Acquisition of high-quality 3D seismic imaging is a critical part of the preinjection site assessment. The use of fault-size analysis prior to injection operations can be an important factor to determine the potential for generating felt seismicity. Estimating the sizes of faults in the population that are likely to slip can be done, if preinjection seismic imaging is of sufficient quality to identify a representative fault population. The injection-induced seismicity clusters indicate additional fault locations, some of which partially coincide with the microseismicity. If interpretable faults in the target reservoir are small (a few hundred meters or less in length or radius), the potential for felt seismicity is more unlikely than in a reservoir with numerous interpretable large faults with lengths of several kilometers and more. Interpretable faults in the Dallas–Fort Worth basin are significantly larger than in the Illinois basin. Hennings *et al.* (2019) stated that induced seismicity in the Dallas–Fort Worth basin is associated with many faults less than 8 km long. Several significant injection-induced earthquake sequences with events $M_w > 2.5$ occurred on smaller faults with trace lengths ranging from about 3 to 6 km (see fig. 5 in Horne *et al.*, 2020). These faults also are mapped with a longer width-to-depth aspect ratio, in which the longer dimension is 6 to over 10 km.

The detailed geometry of the IBDP microseismicity cluster 4 and nearby interpreted faults suggests that it is composed of multiple shorter fault segments of different orientations, and that larger events could occur on a single fault plane with the same dimensions as the cluster. Nearby historical events up to M_w 2.7 could be considered a baseline to predict potential induced event magnitudes for the IBDP area. This study suggests that the absence of historical seismicity $M_w > 3$ in the vicinity and the presence of relatively small mapped fault sizes indicates the induced seismicity detected at the IBDP site may not necessarily be a precursor to the development of felt seismicity. However, injection periods of a few years may not be long enough to fully assess the impact of long-term injection from multiple wells at rates required for commercial carbon dioxide sequestration. High-quality seismic imaging prior to commencing injection operations would allow an a priori assessment of potential seismic hazard, but even when such data are available, identifying the relevant faults in the imaging can still be challenging. This integration of pressure, microseismic, and reservoir properties data at the IBDP demonstrates how a detailed geological characterization of the reservoir

can be applied to mitigate seismic hazard during project development and operation.

DATA AND RESOURCES

Seismograms used in this study were collected by the U.S. Geological Survey (USGS) and the Illinois State Geological Survey (ISGS). The data collected by the USGS can be obtained from the Incorporated Research Institutions for Seismology (IRIS) Data Management Center at www.iris.edu (last accessed July 2019). Seismograms, active seismic data, and well log data collected by the ISGS are not yet publicly available, but they will be accessible after June 2021 through the U.S. Department of Energy (DOE) Energy Data eXchange (EDX) platform (https://www.netl.doe.gov/edx, last accessed May 2020). Additional information about the Move structural analysis and modeling software, which was used to analyze interpreted faults and event-source mechanisms, is available at http://www.petex.com/products/move-suite/ (last accessed June 2020). The supplemental material available online only includes the source mechanisms for the 50 events analyzed, example waveforms, additional porosity version cross sections, and a well-log cross section.

ACKNOWLEDGMENTS

This project is funded by the U.S. Department of Energy through the National Energy Technology Laboratory (NETL), under Agreement DE-FC26-05NT42588, and by CLIMIT (a Norwegian national program that provides financial support for research, development and demonstration of CCS technologies) and the Norwegian Research Council. The authors would like to thank the U.S. Geological Survey (USGS) for providing their event catalog and useful discussions concerning the data. Expert reprocessing of the 3D seismic volume was done by Sterling Seismic Services, and the authors wish to thank them for informative discussions on their seismic reprocessing results. The authors would like to thank Petroleum Experts Ltd. for their kind donation of the MOVE structural analysis software suite used in this study. The authors would also like to thank Schlumberger for their donation of Petrel software, which was used to model and analyze the seismic data for this project.

REFERENCES

Abercrombie, R. E. (1995). Earthquake source scaling relationships from −1 to 5 M_L using seismograms recorded at 2.5-km depth, *J. Geophys. Res.* **100,** no. B12, doi: 10.1029/95jb02397.

Barbour, A. J., J. H. Norbeck, and J. L. Rubinstein (2017). The effects of varying injection rates in Osage county, Oklahoma, on the 2016 M_w 5.8 Pawnee earthquake, *Seismol. Res. Lett.* **88,** no. 4, 1040–1053, doi: 10.1785/0220170003.

Bauer, R. A., R. Will, S. E. Greenberg, and S. G. Whittaker (2019). Illinois Basin–Decatur Project, in *Geophysics and Geosequestration*, T. L. Davis, M. Landro, and M. Wilson (Editors), Chapter 19, Cambridge University Press, Cambridge, United Kingdom, 377 pp.

Benoit, E. L. (1958). The Desmoinesian Series, Edmond Area, Central Oklahoma, *Shale Shaker Digest* **8,** no. 2, 338–349.

Couëslan, M. L., R. Butsch, R. Will, and R. A. Locke (2014). Integrated reservoir monitoring at the Illinois Basin–Decatur Project, *Energy Procedia* **63,** 2836–2847.

Couëslan, M. L., J. Gulati, A. Campbell, and L. Nutt (2013). Monitoring CO2 Injection at the Illinois Basin–Decatur Project with time-lapse 3D VSPs, *Second EAGE Workshop on Borehole Geophysics*, European Association of Geoscientists & Engineers, St. Julian's, Malta, April 2013, doi: 10.3997/2214-4609.20142571.

Couëslan, M. L., V. Smith, G. El-Kaseeh, J. Gilbert, N. Preece, L. Zhang, and J. Gulati (2014). Development and implementation of a seismic characterization and CO2 monitoring program for the Illinois Basin–Decatur Project, *Greenh. Gases Sci. Technol.* **4,** no. 5, 626–644, doi: 10.1002/ghg.1452.

Dawers, N. H., M. H. Anders, and C. H. Scholz (1993). Growth of normal faults: Displacement-length scaling, *Geology* **21,** no. 12, 1107–1110, doi: 10.1130/0091-7613(1993)021<1107:gonfdl>2.3.co;2.

Dohmen, T., J. Zhang, L. Barker, and J. P. Blangy (2017). Microseismic magnitudes and *b*-values for delineating hydraulic fracturing and depletion, *SPE J.* **22,** no. 5, 1624–1634, doi: 10.2118/186096-pa.

Duchek, A. B., J. H. McBride, W. J. Nelson, and H. E. Leetaru (2004). The Cottage Grove fault system (Illinois basin): Late Paleozoic transpression along a Precambrian crustal boundary, *Bull. Geol. Soc. Am.* **116,** nos. 11/12, 1465–1484, doi: 10.1130/B25413.1.

Eisner, L., B. J. Hulsey, P. Duncan, D. Jurick, H. Werner, and W. Keller (2010). Comparison of surface and borehole locations of induced seismicity, *Geophys. Prospect.* doi: 10.1111/j.1365-2478.2010.00867.x.

Freiburg, J. T., J. H. McBride, D. H. Malone, and H. E. Leetaru (2020). Petrology, geochronology, and geophysical characterization of Mesoproterozoic rocks in central Illinois, USA, *Geosci. Front.* **11,** no. 2, 581–596, doi: 10.1016/j.gsf.2019.07.004.

Freiburg, J. T., D. G. Morse, H. E. Leetaru, R. P. Hoss, and Q. Yan (2014). *A depositional and diagenetic characterization of the Mt. Simon sandstone at the Illinois Basin–Decatur Project carbon capture and storage site, Decatur, Illinois, USA*, *Ill. State Geo. Surv. Circular 583*, available at https://isgs.illinois.edu/sites/isgs/files/files/publications/c583.pdf (last accessed July 2020).

Frohlich, C. (2012). A survey of earthquakes and injection well locations in the Barnett Shale, Texas, *Leading Edge* **31,** no. 12, 1446–1451, doi: 10.1190/tle31121446.1.

Frohlich, C., J. I. Walter, and J. F. W. Gale (2015). Analysis of transportable array (USArray) data shows earthquakes are scarce near injection wells in the Williston basin, 2008–2011, *Seismol. Res. Lett.* **86,** no. 2A, 492–499, doi: 10.1785/0220140180.

Goertz-Allmann, B. P., S. J. Gibbons, V. Oye, R. A. Bauer, and R. Will (2017). Characterization of induced seismicity patterns derived from internal structure in event clusters, *J. Geophys. Res.* **122,** no. 5, 3875–3894, doi: 10.1002/2016JB013731.

Goertz-Allmann, B. P., D. Kühn, V. Oye, B. Bohloli, and E. Aker (2014). Combining microseismic and geomechanical observations to interpret storage integrity at the In Salah CCS site, *Geophys. J. Int.* **198,** no. 1, 447–461, doi: 10.1093/gji/ggu010.

Gudmundsson, A., G. De Guidi, and S. Scudero (2013). Length–displacement scaling and fault growth, *Tectonophysics* **608,** 1298–1309, doi: 10.1016/j.tecto.2013.06.012.

Hanks, T. C., and H. Kanamori (1979). A moment magnitude scale, *J. Geophys. Res.* **84,** no. B5, 2348–2350, doi: 10.1029/JB084iB05p02348.

Hennings, P. H., J. E. L. Snee, J. L. Osmond, H. R. Deshon, R. Dommisse, E. Horne, C. Lemons, and M. D. Zoback (2019). Injection-induced seismicity and fault-slip potential in the fort

Worth basin, Texas, *Bull. Seismol. Soc. Am.* **109,** no. 5, 1615–1634, doi: 10.1785/0120190017.

Holloway, S., A. Holland, and G. R. Keller (2016). Oklahoma fault database contributions from the oil and gas industry, *Oklahoma Geol. Surv. Open-File Rept. OF1-2016*, available at http://ogs.ou.edu/docs/openfile/OF1-2016P1.pdf (last accessed July 2020).

Hollrah, T. L. (1979). Subsurface lithostratigraphy of the Hunton Group, in parts of Payne, Lincoln and Logan Counties, Oklahoma, *Shale Shaker Digest* **29**, no. 9, 76–91.

Horne, E., P. H. Hennings, J. L. Osmond, and H. R. Deshon (2020). Structural characterization of potentially seismogenic faults in the fort worth basin, *Interpretation* **8,** doi: 10.1190/int-2019-0188.1.

Horton, S. (2012). Disposal of hydrofracking waste fluid by injection into subsurface aquifers triggers earthquake swarm in central Arkansas with potential for damaging earthquake, *Seismol. Res. Lett.* **83,** no. 2, 250–260, doi: 10.1785/gssrl.83.2.250.

Kaven, J. O., S. H. Hickman, A. F. McGarr, and W. L. Ellsworth (2015). Surface monitoring of microseismicity at the Decatur, Illinois, CO_2 sequestration demonstration site, *Seismol. Res. Lett.* **86,** no. 4, 1096–1101, doi: 10.1785/0220150062.

Kaven, J. O., S. H. Hickman, A. F. McGarr, S. Walter, and W. L. Ellsworth (2014). Seismic monitoring at the Decatur, IL, CO_2 sequestration demonstration site, *Energy Procedia* **63,** 4264–4272, doi: 10.1016/j.egypro.2014.11.461.

Kwiatek, G., K. Plenkers, and G. Dresen (2011). Source parameters of picoseismicity recorded at Mponeng deep gold mine, South Africa: Implications for scaling relations, *Bull. Seismol. Soc. Am.* **101,** no. 6, 2592–2608, doi: 10.1785/0120110094.

Lahann, R. W., J. A. Rupp, C. R. Medina, G. Carlson, and K. M. Johnson (2017). State of stress in the Illinois Basin and constraints on inducing failure, *Environ. Geosci.* **24,** 123–150.

Langet, N., B. Goertz-Allmann, V. Oye, R. A. Bauer, S. Williams-Stroud, A. M. Dichiarante, and S. E. Greenberg (2020). Joint focal mechanism inversion using downhole and surface monitoring at the Decatur, Illinois, CO2 injection site, *Bull. Seismol. Soc. Am.* 1–20, doi: 10.1785/0120200075.

Leetaru, H. E., and J. T. Freiburg (2014). Litho-facies and reservoir characterization of the Mt Simon Sandstone at the Illinois Basin - Decatur Project, *Greenh. Gases Sci. Technol.* **4,** 580–595, doi: 10.1002/ghg.1453.

Magnani, M. B., M. L. Blanpied, H. R. DeShon, and M. J. Hornbach (2017). Discriminating between natural versus induced seismicity from long-term deformation history of intraplate faults, *Sci. Adv.* **3,** no. 11, e1701593, doi: 10.1126/sciadv.1701593.

Martin Mai, P., and G. C. Beroza (2000). Source scaling properties from finite-fault-rupture models, *Bull. Seismol. Soc. Am.* **90,** no. 3, 604, doi: 10.1785/0119990126.

McBride, J. H., R. W. Keach, H. E. Leetaru, and K. M. Smith (2017). Visualizing Precambrian basement tectonics beneath a carbon capture and storage Site, Illinois basin, *Interpretation* **6,** no. 2, 1–14, doi: 10.1190/int-2017-0116.1.

McBride, J. H., H. E. Leetaru, R. W. Keach, and E. I. McBride (2016). Fine-scale structure of the Precambrian beneath the Illinois basin, *Geosphere* **12,** no. 2, 585–606, doi: 10.1130/GES01286.1.

McGarr, A., and J. B. Fletcher (2003). Maximum slip in earthquake fault zones, apparent stress, and stick-slip friction, *Bull. Seismol. Soc. Am.* **93,** no. 6, 2355–2362, doi: 10.1785/0120030037.

Miller, H. J. (1956). The Oklahoma earthquake of April 9, 1952, *Bull. Seismol. Soc. Am.* **46,** no. 4, 269–279.

Palkovic, M. J. (2015). Depositional characterization of the Eau Claire formation at the Illinois Basin–Decatur Project: Facies, mineralogy and geochemistry, *M.S. Thesis*, University of lllinois at Urbana-Champaign, Champaign, lllinois.

Peyret, O., J. Drew, M. Mack, K. Brook, S. Maxwell, and C. Cipolla (2012). Subsurface to surface microseismic monitoring for hydraulic fracturing, *SPE Annual Technical Conf. and Exhibition*, San Antonio, Texas, 8–10 October, SPE 159670.

Potter, C. J., J. A. Drahovzal, M. L. Sargent, and J. H. McBride (1997). Proterozoic structure, Cambrian rifting, and younger faulting as revealed by a regional seismic reflection network in the southern Illinois basin, *Seismol. Res. Lett.* **68,** no. 4, 537–552, doi: 10.1785/gssrl.68.4.537.

Rinaldi, A. P., J. Rutqvist, and F. Cappa (2014). Geomechanical effects on CO_2 leakage through fault zones during large-scale underground injection, *Int. J. Greenh. Gas Control* **20,** 117–131, doi: 10.1016/j.ijggc.2013.11.001.

Rotevatn, A., and H. Fossen (2011). Simulating the effect of subseismic fault tails and process zones in a siliciclastic reservoir analogue: Implications for aquifer support and trap definition, *Mar. Pet. Geol.* **28,** no. 9, 1648–1662, doi: 10.1016/j.marpetgeo.2011.07.005.

Scales, M. M., H. R. DeShon, M. B. Magnani, J. I. Walter, L. Quinones, T. L. Pratt, and M. J. Hornbach (2017). A decade of induced slip on the causative fault of the 2015 M_w 4.0 Venus earthquake, northeast Johnson County, Texas, *J. Geophys. Res.* **122**, no. 10, 7879–7894, doi: 10.1002/2017JB014460.

Scanlon, B. R., R. C. Reedy, M. B. Weingarten, and K. E. Murray (2019). Managing basin-scale fluid budgets to reduce injection-induced seismicity from the recent U.S. Shale oil revolution, *Seismol. Res. Lett.* **90,** no. 1, 171–182, doi: 10.1785/0220180223.

Shaw, B. E., and C. H. Scholz (2001). Slip-length scaling in large earthquakes: Observations and theory and implications for earthquake physics, *Geophys. Res. Lett.* **28,** no. 15, 2995–2998, doi: 10.1029/2000GL012762.

Skoumal, R. J., M. R. Brudzinski, and B. S. Currie (2015). Microseismicity induced by deep wastewater injection in southern Trumbull County, Ohio, *Seismol. Res. Lett.* **86,** no. 5, 1326–1334, doi: 10.1785/0220150055.

Smith, V., and P. Jaques (2016). Illinois Basin–Decatur Project pre-injection microseismic analysis, *Int. J. Greenh. Gas Control* **54,** 362–377, doi: 10.1016/J.IJGGC.2015.12.004.

Stork, A. L., J. P. Verdon, and J. M. Kendall (2014). The robustness of seismic moment and magnitudes estimated using spectral analysis, *Geophys. Prospect.* **62,** no. 4, 862–878, doi: 10.1111/1365-2478.12134.

Thingbaijam, K. K. S., P. Martin Mai, and K. Goda (2017). New empirical earthquake source-scaling laws, *Bull. Seismol. Soc. Am.* **107,** no. 5, 2225–2246, doi: 10.1785/0120170017.

van der Baan, M., and F. J. Calixto (2017). Human-induced seismicity and large-scale hydrocarbon production in the USA and Canada, *Geochem. Geophys. Geosyst.* **18,** 2467–2485, doi: 10.1002/2017GC006915.

Verdon, J. P. (2016). Using microseismic data recorded at the Weyburn CCS-EOR site to assess the likelihood of induced seismic

activity, *Int. J. Greenh. Gas Control* **54,** 421–428, doi: 10.1016/j.ijggc.2016.03.018.

Walsh, F. R., and M. D. Zoback (2016). Probabilistic assessment of potential fault slip related to injection-induced earthquakes: Application to north-central Oklahoma, USA, *Geology* **44,** no. 12, 991–994, doi: 10.1130/G38275.1.

Weingarten, M., S. Ge, J. W. Godt, B. A. Bekins, and J. L. Rubinstein (2015). High-rate injection is associated with the increase in U.S. mid-continent seismicity, *Science* **348,** no. 6241, 1336–1340, doi: 10.1126/science.aab1345.

Wells, D. L., and K. J. Coppersmith (1994). New empirical relationships among magnitude, rupture length, rupture width, rupture area, and surface displacement, *Bull. Seismol. Soc. Am.* **84,** no. 4, 974–1002.

White, J. A., L. Chiaramonte, S. Ezzedine, W. Foxall, Y. Hao, A. Ramirez, and W. McNab (2014). Geomechanical behavior of the reservoir and caprock system at the In Salah CO_2 storage project, *Proc. Natl. Acad. Sci. Unit. States Am.* **111,** no. 24, 8747–8752, doi: 10.1073/pnas.1316465111.

Williams-Stroud, S., C. Ozgen, and R. L. Billingsley (2013). Microseismicity-constrained discrete fracture network models for stimulated reservoir simulation, *Geophysics* **78,** no. 1, B37–B47, doi: 10.1190/geo2011-0061.1.

Manuscript received 6 March 2020
Published online 18 August 2020